Wind Tunnel Tests of a Thick Wind Turbine Airfoil

Mouton, Sylvain; Peter Schaffarczyk, Alois; Timmer, Nando

DOI
10.1002/we.2938

Publication date
2024

Document Version
Final published version

Published in
Wind Energy

Citation (APA)
Mouton, S., Peter Schaffarczyk, A., & Timmer, N. (2024). Wind Tunnel Tests of a Thick Wind Turbine Airfoil. *Wind Energy*, *27*(10), 994-1010. https://doi.org/10.1002/we.2938

Wind Energy

WILEY

RESEARCH ARTICLE OPEN ACCESS

Wind Tunnel Tests of a Thick Wind Turbine Airfoil

Sylvain Mouton[1] | Alois Peter Schaffarczyk[2] | Nando Timmer[3]

[1]Wind Tunnels Department, ONERA, Mauzac, France | [2]Department of Mechanical Engineering, Kiel University of Applied Sciences, Kiel, Germany | [3]Faculty of Aerospace Engineering, Delft University of Technology, Delft, The Netherlands

Correspondence Sylvain Mouton (sylvain.mouton@onera.fr)

Received: 24 November 2023 | **Revised:** 13 May 2024 | **Accepted:** 9 June 2024

Funding: This work was funded by ONERA's research budget as part of the continual improvement of its wind-tunnel testing services.

Keywords: thick airfoil aerodynamics | wind tunnel testing

ABSTRACT

This article reports about a wind-tunnel experiment carried out in the ONERA F2 low-speed wind tunnel on a model of the DU 97-W-300Mod airfoil designed for wind turbine application. The wind tunnel, the airfoil model, and experimental techniques used are presented, with special emphasis on the data processing and corrections required to derive airfoil forces and pressure distribution. To better document the flow physics at play, the results are illustrated by infrared thermography and surface oil flow visualization. The test allowed investigating Reynolds number effects between 1 and 3.8 millions. To ameliorate the understanding of the benefits and limitations of such airfoil testing, one section is devoted to the comparison of present results with previous experiments in other wind tunnels. Some of the difficulties arising in airfoil testing are evidenced and discussed to contribute to the improvement of test methods.

1 | Introduction

The development of large wind turbines in the last decades has prompted the creation of new airfoil shapes, dedicated to high-aspect ratio blades, whose design point and characteristics are different from existing airfoils. In particular, these airfoils are generally much thicker, with thickness-to-chord ratios in the order of 20% to 50%, making them more sensitive to early separation of the boundary layer. As wind turbine size increases, the operational Reynolds number of these airfoils also increases to reach several millions. There are even specific pre-designs using 250-m long blades [1], in which the Reynolds number based on maximum chord (16 m) will reach 20 million.

In the development of these new airfoils, experimental data are required to validate aerodynamic design [2], even more when these airfoils are affected by roughness, erosion or icing [3] or get equipped with various flow control devices, such as vortex generators [4, 5] or riblets [6]. These small details are indeed difficult to simulate as they imply small scale physics in the boundary layer. Airfoil thickness also adds complexity to the flow because of increased pressure gradients. Above a certain amount of thickness, the aerodynamic behavior may change very drastically [6]. This adverse effects seems to be closely related to the onset of massive—sometimes asymmetric (upper vs. lower side)—flow separation. These effects, however, generally occur at thicknesses far above the 30% thickness considered here. Meeting this experimental need was not as straightforward as one might have thought by considering past decades of wind tunnel testing, and some new wind tunnels were even built [2] for that purpose. The proper 2D aerodynamic testing of an airfoil is actually far from simple for different reasons, some of which will be discussed in this paper. For that reason, it is always wise to cross-compare results from different wind tunnels.

This paper reports about an experiment on a 30% thick profile, called DU 97-W-300Mod, tested in the ONERA F2 wind-tunnel. The wind-tunnel and airfoil model are presented in Section 2. Experimental techniques and data processing are introduced in Section 3. Section 4 presents results about airfoil performance, including force coefficients, pressure distributions and boundary layer transition. The impact of variation

in Reynolds number is examined. Section 5 is devoted to the comparison of the present data set with previously published results on the same or a very similar airfoil. Throughout the paper, difficulties that can arise in thick airfoil testing are underlined [7, 8].

2 | Wind Tunnels and Airfoil Models

This section introduces the DU 97-W-300 airfoil and the modified version DU 97-W-300Mod. It also presents in Section 2.2 the ONERA F2 wind-tunnel that was used for the present experiment. Since these results will be compared with those obtained in other wind tunnels, Sections 2.3 and 2.4 briefly present the main features of these previous experiments, while details can be found in the original publications cited.

2.1 | The DU 97-W-300Mod Airfoil

Aerodynamic design of wind turbine blades [9] is a strong iterative and inter-related process within a complete wind turbine design with very few detailed information outside manufacturers. Fortunately, in the past couple of years, so-called *reference turbine designs* were published, one of the most recent being a 15-MW rated power turbine with a 240-m rotor diameter [10].

For the generic blade aerodynamic design, in combination with chord and twist, airfoils have to be specified in span-wise direction. In the beginning, airfoils designed for low-speed aeronautical application were used, but around the 1990s, special wind turbine dedicated airfoils have been designed, among which a DU-airfoil family designed at TU Delft [11, 12].

The airfoil tested here is a modification of the 30% thick DU 97-W-300, called DU 97-W-300Mod [11]. It has a trailing edge thickness of 0.492%, much thinner than the 1.74% of the original airfoil. The same modified profile shape was used in the DOWEC-project [13] and in the design of the NREL 5 MW turbine blade under the name DU 97-W-300LM [14]. Original DU 97-W-300 data come from measurements in the TU Delft low-turbulence wind tunnel (described in Section 2.4). The airfoil was under recent study in [4, 5] where it was fitted with vortex generators. The modified airfoil was previously tested in the KKK wind tunnel in Cologne (Section 2.3) and in the wind tunnel of Deutsche Windguard [15] where it was equipped with riblets. Another DU-profile, DU 00-W-210 (of 21% thickness), was tested to Reynolds number impact and varying inflow turbulence [16].

2.2 | Experiment in the ONERA F2 Wind Tunnel

The F2 wind tunnel is a low-speed low-turbulence atmospheric wind tunnel fully described in [17, 18]. It has a closed return circuit operated at atmospheric pressure. The flow is driven by a variable speed electric motor of 700 kW. It features a rectangular test section (1.4 m wide × 1.8 m high × 5 m long) that can be equipped with large transparent wall panels, and it is surrounded by a three-degree-of-freedom traverse system. This makes the F2 particularly well suited for the use of optical measurement systems, for example, as in [19]. The maximum velocity is about 100 m/s. When testing models producing exceptionally high drag, the pitch angle of the fan blades can be reduced to avoid fan surge, but this was not necessary for the test reported in this article. A combination of screens, honeycombs and a contraction ratio of 12 contribute to a low turbulence level ranging from 0.03% at 20 m/s to 0.05% at 100 m/s (over 5-Hz to 5-kHz frequency band). The floor and ceiling are made slightly divergent to compensate for the growth of the boundary layers on the wind tunnel walls. Therefore, the static pressure in the volume of the test section is homogeneous within 0.25% of the dynamic pressure. The wind tunnel velocity is measured using a reference total pressure probe and a reference total temperature probe, both located in the settling chamber, as well as two reference static pressure taps located on the floor and ceiling, shortly after the entrance of the test section. Wind-tunnel calibration showed that the flow conditions in the test section are equal to these reference flow conditions, within 0.5% of the velocity.

The airfoil model has a chord of 600 mm, is mounted horizontally and spans the entire breadth of the wind-tunnel; see Figures 1 and 2. It was machined out of aluminum with an accuracy everywhere better than 0.1 mm, that is, 0.017% of chord and a surface roughness $R_a < 0.8\,\mu\text{m}$. It is equipped with 62 static pressure taps of 0.3 m diameter, located on an mechanical insert at mid-span. A configuration using zigzag tape to trigger transition on the suction side of the airfoil was also tested. Finally, a configuration with vortex generators identical to the *Base design* configuration of [4] was measured. For the sake of brevity, results on these last two configurations are not reported on this paper.

The wake rake has a width of 400 mm and is equipped with 80 total pressure tubes (hole diameter 0.8 mm) 5 mm apart and 21 static pressure tubes 20 mm apart. During most of the experiment, it was positioned in the wake of the airfoil 480 mm (0.8 chord) downstream of the trailing edge. A traverse system allowed to translate the rake in all directions. When slowly pitching the airfoil, the vertical position of the rake was also continuously adjusted to follow the position of the wake. This traverse system was also used to investigate the dependency of drag measurement with the span-wise position in Section 4.3.

2.3 | Experiment in the DNW-KKK Wind Tunnel

These wind tunnel tests already reported in [20] were performed in the DNW cryogenic wind tunnel Kryo-Kanal Köln (KKK) in Cologne, Germany, in 2002 and repeated in 2003. This wind tunnel, which was dismantled in 2020, had a closed single-return atmospheric circuit with a 1 MW drive and a square test section of $2.4 \times 2.4\ \text{m}^2$. The high Reynolds numbers are reached by injection of liquid nitrogen into the flow, which could cool the tunnel gas down to less than 100 K (−170°C) while reducing its viscosity significantly.

The wind tunnel model had a chord of 500 mm, was mounted vertically and completely spanned the test section. It was equipped with 62 pressures taps staggered near mid-span that were measured with PSI pressure modules. A wake rake, with a total of 58 pressure tubes, was positioned 750 mm (1.5 chord)

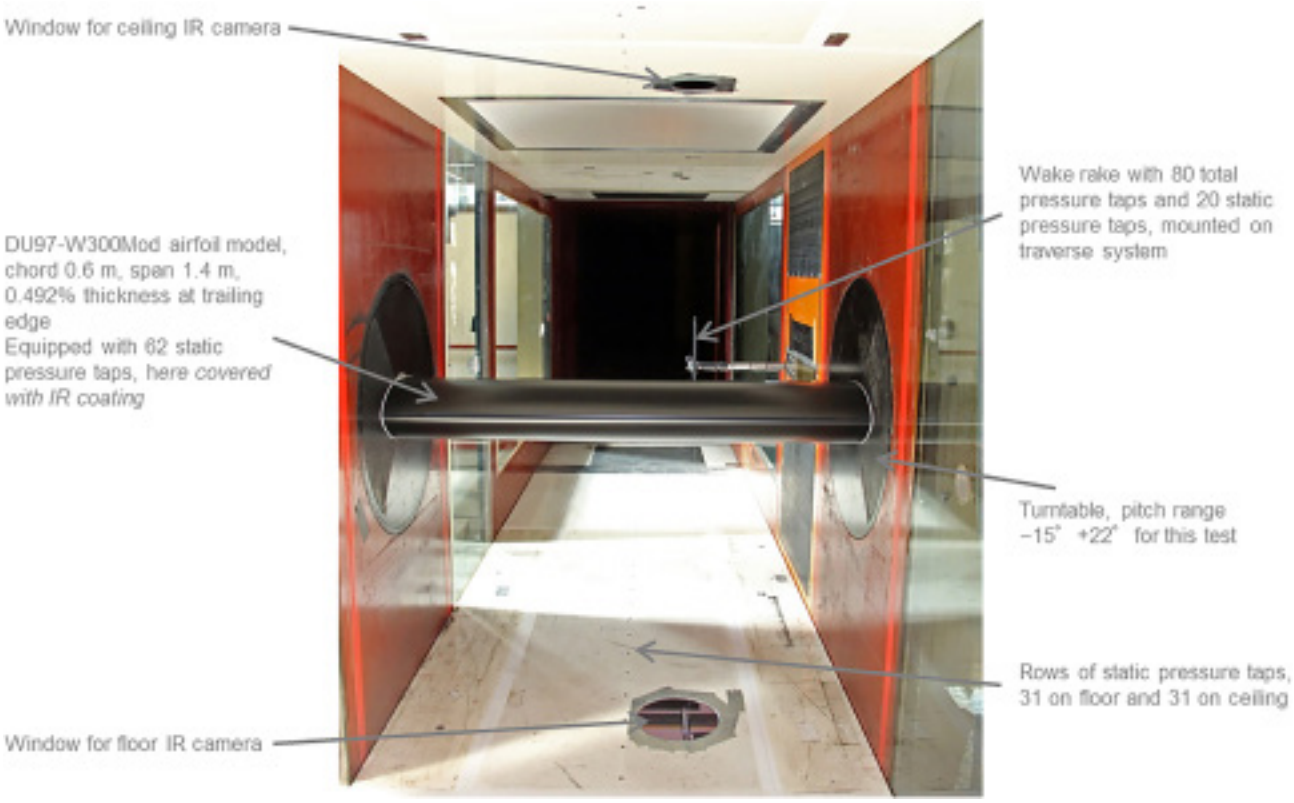

FIGURE 1 | General view of the wind tunnel experiment.

downstream of the trailing edge. Wind tunnel wall corrections given in [21] have been applied.

2.4 | Experiment in the TU Delft Wind Tunnel

The tests on the original DU 97-W-300 airfoil were performed in the Delft University of Technology (TUD) atmospheric low-speed low-turbulence wind tunnel (LTT). The tunnel is of the closed, single return type with a contraction ratio of 17.8. In combination with five turbulence screens in the plenum chamber, the longitudinal turbulence intensity in the 1.25 m (height) × 1.80 m (width) × 2.60 m (length) octagonal test section varies from 0.017% at 10 m/s to 0.04% at 80 m/s. The airfoil model had a chord of 0.65 m and completely spanned the test section height. Some early test results, including the effect of zigzag tape and vortex generators, have been reported in [11, 22]. An extensive study on the impact of the size and location of vortex generators on this airfoil has been performed by Baldacchino [4]. This airfoil model was modified in [23] with a lower surface add-on to study the impact of a 10% flatback combined with a so-called swallow tail. Drag measurements are performed with a 504-mm-wide wake rake containing 16 static and 67 total pressure tubes. The wake rake can be traversed along as well as normal to the trailing edge at a typical distance of 80% of the chord behind the model. Measurements are corrected for the presence of the wind tunnel walls, including second order terms for lift interference according to [21]. The complete set of correction equations is presented in [24].

3 | Testing Techniques

3.1 | Wind Tunnel Flow Conditions

The F2 wind tunnel test section is kept at approximately atmospheric pressure and temperature. An increase in velocity causes an increase in both Mach M_0 and Reynolds Re_0 numbers. At low Mach number, it is often assumed that Mach number effects are negligible, so that in most of the following figures, only the Reynolds number is reported. The experiment was carried out in order to match the uncorrected Reynolds numbers provided in Table 1. Depending on the atmospheric pressure and temperature of the day, the corresponding velocity and Mach number could slightly change.

In F2, tunnel velocity is measured using two static pressure taps, one on the floor, one on the ceiling, located near the entrance of the test section. Differential pressure sensors are used to measure their static pressure with reference to the total pressure on a Pitot tube in the settling chamber. Two redundant Drück sensors of ±1 psi range (±7 kPa) are used for each tap, as most of the uncertainty in dynamic pressure stems from this differential pressure measurement. The readings of the two reference taps are averaged to eliminate lift interference on the taps. The total pressure is measured against local atmospheric pressure using another Drück ±1 psi differential pressure sensor, and the absolute atmospheric pressure is measured with a Drück RPT 301 sensor. This setup results in an uncertainty of the dynamic pressure q_0 of about 7 Pa.

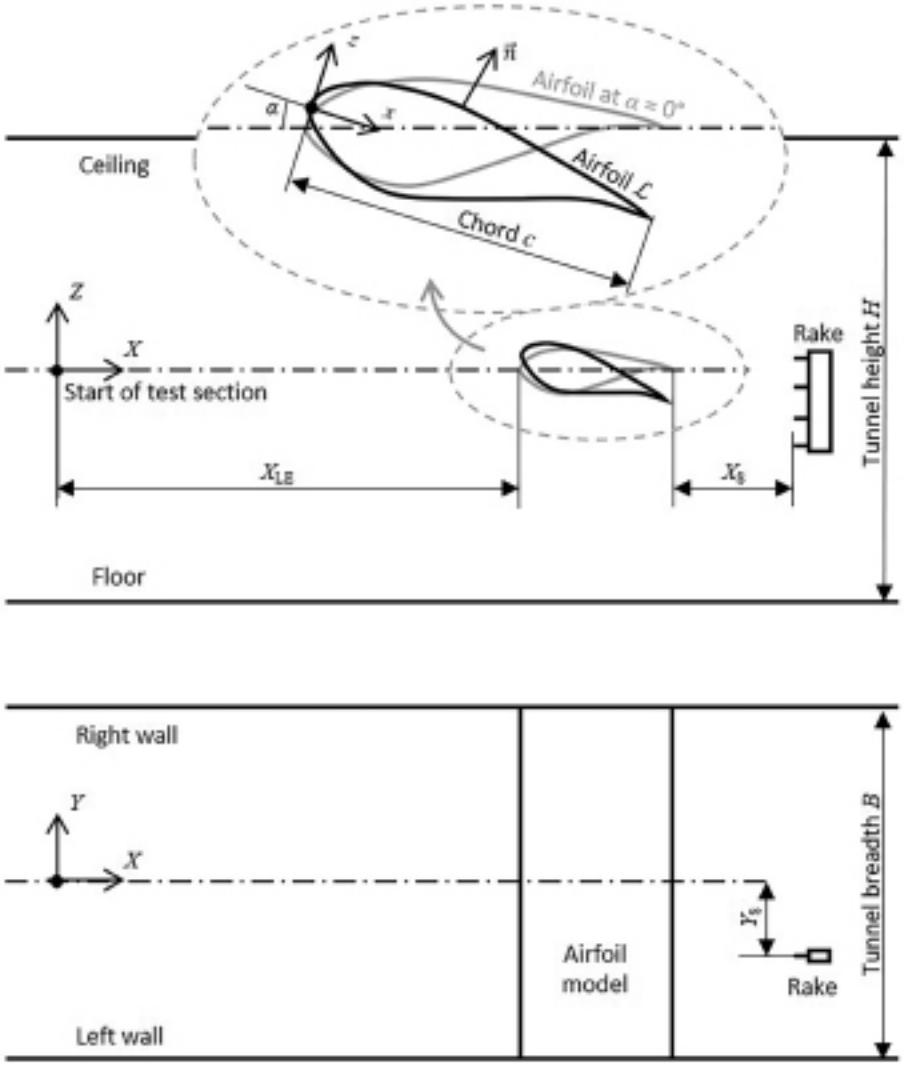

FIGURE 2 | Schematic of the wind tunnel experiment, with main geometrical notations indicated.

TABLE 1 | Tunnel flow conditions during experiment.

Reynolds number Re_0	Mach number M_0	Velocity V_0	Relative uncertainty on q_0
1.0×10^6	≈ 0.08	≈ 26 m/s	1.7%
2.0×10^6	≈ 0.15	≈ 52 m/s	0.42%
3.0×10^6	≈ 0.23	≈ 77 m/s	0.19%
3.7×10^6	≈ 0.28	≈ 95 m/s	0.13%

3.2 | Airfoil Angle of Attack

The airfoil pitch angle is measured with a Honeywell Q-Flex QA-2000 accelerometer positioned on the right side of the model, outside the wind-tunnel flow. The uncertainty in pitch angle is lower than 0.01°. The mean upwash angle in the test section is below 0.1° according to available knowledge and is neglected. Therefore, the uncorrected angle of attack α is simply the airfoil pitch angle. During most of the experiment reported here, the airfoil was pitched up from $\alpha = -15°$ to $+22°$ at a rate of 0.3°/s (upward pitch-sweep run) and then pitched down at -0.3°/s (downward pitch-sweep run). Data were acquired at 500 Hz with an appropriate analog anti-aliasing filter and then numerically filtered and down-sampled at 5 Hz.

3.3 | Airfoil Pressure Measurement

The airfoil is equipped with 62 pressure taps. Their manufacturing technique and diameter were chosen to avoid the different possible bias reported in [25], and that were encountered by [26] in the field of wind turbine airfoil testing. Pressure

measurements were carried out using a PSI ESP-64HD electronic pressure scanners of ±5 psi (±35 kPa) range.

Once pressure data are collected, the pressure force $\vec{F}_p$ on the airfoil is computed by integrating

$$\vec{F}_p = \int_{\mathcal{L}} -p\vec{n}\, ds, \tag{1}$$

where $\vec{n}$ is the outgoing unit vector normal to the airfoil curve $\mathcal{L}$ of length ℓ. To compute this integral, this curve is discretized in curvilinear coordinates $0 \le s < \ell$. The airfoil geometry $\vec{n}(s)$ is known everywhere along this curve, whereas the pressure distribution $p(s)$ is known only at the location of the pressure taps. Therefore, an interpolation of the pressure distribution is required. A linear interpolation was used in the present case, but more elaborate interpolations can be used if needed, depending on the tap location and density. The interpolation accounts for the fact that the pressure distribution is cyclic with $p(\ell) = p(0)$, as the curve $\mathcal{L}$ loops on itself.

3.4 | Wake Rake Pressure Measurement

The rake measurements are composed of static pressure p and stagnation pressure p_i in the wake. They were measured using two PSI ESP-64HD scanners of ±5 psi (±35 kPa) range.

In order to process the rake data, measurements are first interpolated as a function of the vertical coordinates Z; see Figure 3. A cubic spline regression is used, which allows to smooth out variations smaller than the estimated uncertainty in pressure measurement. Nevertheless, drag uncertainty is high at the lowest Reynolds number tested, as the dynamic pressure amounts to only about 1% of the capacity of the pressure sensor of the rake.

Then, the processing of these measurements is based on the *ONERA3* method reported in [27], adapted to the 2D case by assuming that the lateral and vertical velocity are zero at the rake position, and that the total temperature is constant in the flow. It was shown in [27] that this formulation is superior to many others when the Mach number grows and when the wake survey is carried out close to the obstacle. However, in the present case, the early incompressible formulation of Jones [28] estimates drag coefficients that are within 5×10^{-4} of *ONERA3* method, even when ignoring the compressibility effect provided in [29].

3.5 | Wind Tunnel Wall Pressure Measurement and Wall Corrections

The tunnel floor and ceiling are each equipped with 31 pressure taps over a length of about 4.5 m. Pressure was measured using a PSI ESP-64HD scanners of ±1 psi (±7 kPa) range.

A bidimensional flow model, governed by the linearized compressible potential flow equation, is considered to process these wall pressure measurements. This flow model is identical to the one used to derive the classical wall correction for airfoil testing [2, 21, 24, 30]. In this model, the flow field turns out to be the sum of

- the unperturbed flow with a velocity u_0,
- the perturbations induced by the airfoil and
- the perturbations induced by an infinite array of images of the airfoil through the lower and upper wind tunnel walls.

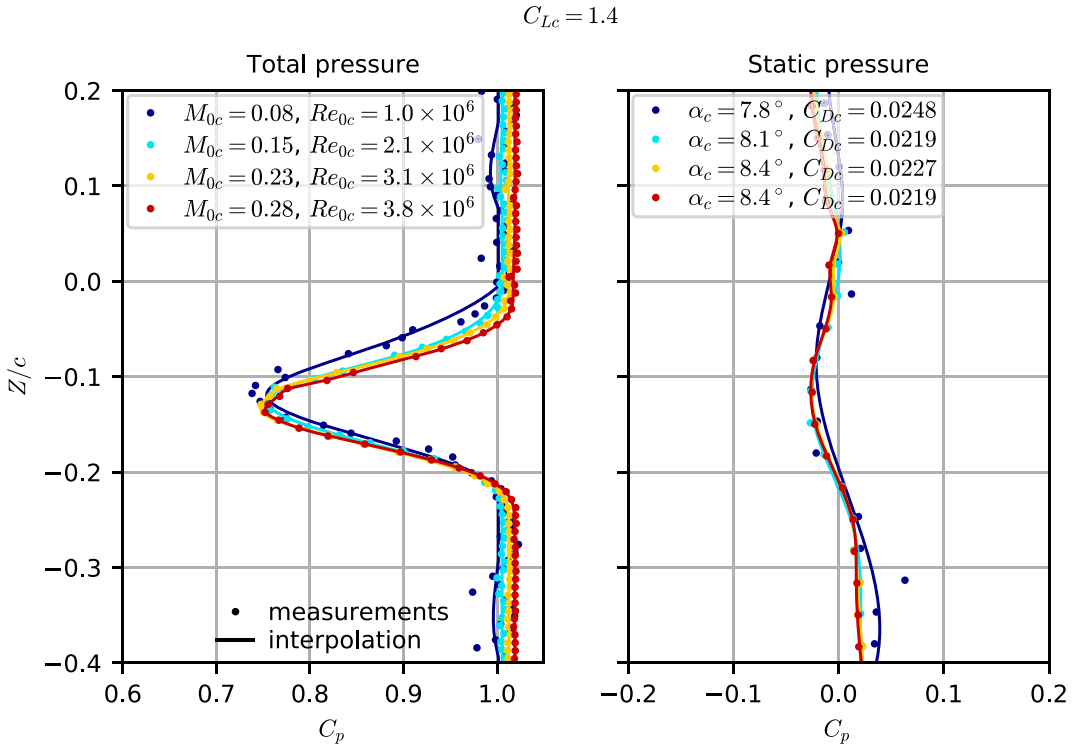

FIGURE 3 | Rake measurement on clean airfoil, for different flow conditions, at a corrected lift coefficient of $C_{Lc} = 1.4$.

Using thin airfoil theory, the perturbation induced by the airfoil can be modelled using only three point singularities:

- a vortex directed along Y with an intensity equal to the total circulation around the airfoil, that is, proportional to the lift per unit span,
- a doublet directed along $-X$ with an intensity proportional to the effective cross-sectional area A of the airfoil and
- a source with an intensity proportional to the drag per unit span.

We limit ourselves here to the case where the airfoil is located at mid-height in the wind tunnel. In this case, the singularities are located at $Z = 0$ and at X_Γ, X_μ and X_σ for the vortex, doublet and source, respectively. Later on, we assume that $X_\mu = X_\sigma$. With C_M defined as the pitching moment coefficient at a reduction point located at one quarter of the chord, the center of lift is located at [21], eq. 2.8

$$\frac{X_\Gamma}{c} = \frac{1}{4} - \frac{C_M}{C_L}. \tag{2}$$

Having set up this flow model, the pressure coefficient on the tunnel walls can be computed as the infinite sum of the images of the above defined singularities. The calculation has been performed in [31] for the incompressible case with no lift. Principles to include compressibility effect have been presented in [21] and the resulting formula in [32], eq. 6.3. The theory is here extended to account for the effect of lift as well.

The pressure coefficient on the floor ($Z = -H/2$) and ceiling ($Z = +H/2$) of the test section $C_{p,\text{wall}}$ is given as a function of X by Equation (3), where the three terms represent, respectively, the effect of solid blockage (modelled with the doublet), wake blockage (modelled with the source) and lift (modelled with the vortex):

$$\begin{aligned} C_{p,\text{wall}}\left(X, Z = \pm\frac{H}{2}\right) = & -\pi\frac{A}{\beta^3 H^2}\frac{1}{\cosh^2\left(\frac{\pi}{\beta}\frac{X-X_\mu}{H}\right)} \\ & -\frac{1}{2}\frac{c}{\beta^2 H}C_D\left(1+\tanh\left(\frac{\pi}{\beta}\frac{X-X_\sigma}{H}\right)\right) \\ & \mp\frac{1}{2}\frac{c}{\beta H}C_L\frac{1}{\cosh\left(\frac{\pi}{\beta}\left(\frac{X-X_{\text{LE}}}{H}+\frac{c}{H}\left(\frac{C_M}{C_L}-\frac{1}{4}\right)\right)\right)}, \end{aligned} \tag{3}$$

where $\beta = \sqrt{1-M_0^2}$ is the compressibility factor, with M_0 the upstream Mach number.

In the present work, a parametric regression of wall measurement was carried out to deduce the five following unknown parameters: $X_\mu = X_\sigma$, A, C_L, C_M and C_D. A least-square gradient-based optimization algorithm is used to minimize the residual difference between the measured distribution of pressure coefficient on floor and ceiling and the one predicted by Equation (3). Examples of result of this regression are shown in Figure 4, and the advantages of this method will be discussed in Sections 4.1 and 4.2. This regression technique is similar in its principle to the one proposed by Allmaras in [33] and used recently in [34].

Once these parameters are evaluated, the wall corrections (lift interference and blockage) can be computed from the classical theory, namely, for the blockage [21], eqs. 5.7 and 5.48:

$$\varepsilon_S = \frac{\pi}{6}\frac{A}{\beta^3 H^2}, \tag{4}$$

$$\varepsilon_W = \frac{1}{4}\frac{c}{\beta^2 H}C_D. \tag{5}$$

The wake blockage ε_W is multiplied by a factor $1+(\gamma-1)M_0^2$ in [35] to account for the effect of compressibility on the intensity of source singularity. At low Mach numbers, this term changes the correction by a few percent only and can be ignored. Higher order terms in $\left(\frac{c}{H}\right)^2$ can also be included [24].

The blockage coefficients in Equations (4) and (5) correspond to the increase in velocity between the infinite upstream and the model location. Since the reference taps in the wind tunnel are not located infinitely far away from the model, the model interference at the reference tap location $(X_{\text{ref}}, Z_{\text{ref}})$ also needs to be taken into account. The interference coefficient ε_R at each reference tap is computed with the help of Equation (3) as

$$\varepsilon_R = -\frac{1}{2}C_{p,\text{wall}}\left(X = X_{\text{ref}}, Z = Z_{\text{ref}}\right). \tag{6}$$

Since the average of two reference taps is used in computing tunnel velocity, ε_R is actually the average of the values computed at each of the tap positions.

The final blockage coefficient ε used to derive the corrected velocity is then

$$\varepsilon = \varepsilon_S + \varepsilon_W - \varepsilon_R. \tag{7}$$

Regarding lift interference, it is responsible for a change in AoA by an amount [21], eq. 2.16:

$$\Delta\alpha = \frac{\pi}{96}\frac{c^2}{\beta H^2}\left(C_L + 4C_M\right). \tag{8}$$

Once upstream flow conditions are properly corrected, there also exist residual corrections to force coefficients [21], eqs. 2.17 and 5.92:

$$\Delta C_L = -\frac{\pi^2}{48}\frac{c^2}{\beta^2 H^2}C_L, \tag{9}$$

$$\Delta C_M = -\frac{\pi^2}{192}\frac{c^2}{\beta^2 H^2}C_L, \tag{10}$$

$$\Delta C_D = -\varepsilon_S C_D. \tag{11}$$

These corrective terms are then used to compute corrected flow conditions as explained in [21], for example, the corrected velocity is $V_{0c} = (1+\varepsilon)V_0$, and the corrected AoA is $\alpha_c = \alpha + \Delta\alpha$. Forces are reduced to non-dimensional coefficients

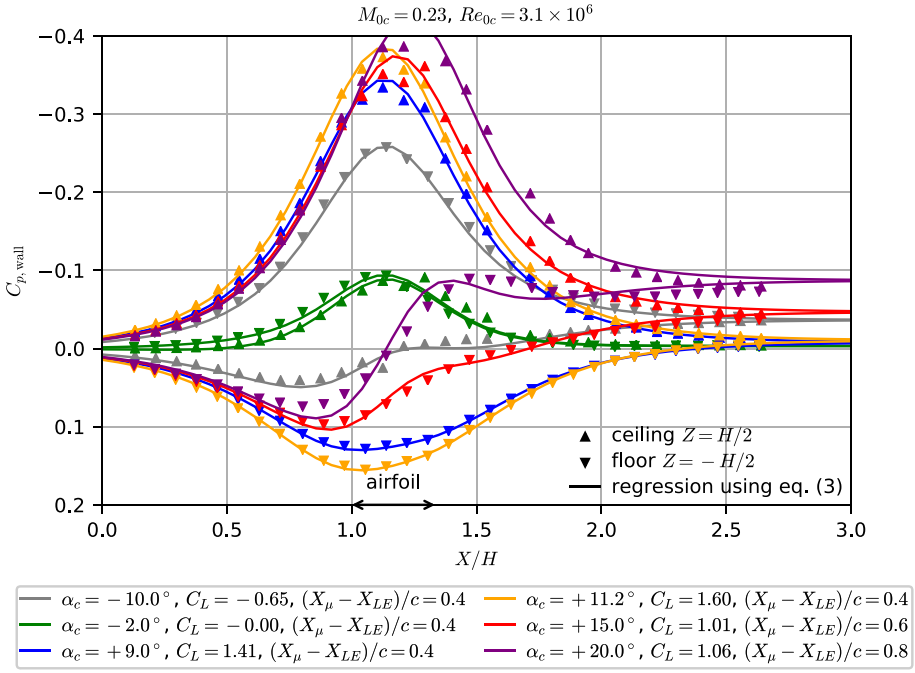

FIGURE 4 | Wall pressure measurements and result of parametric regression for different AoA.

using corrected dynamic pressure q_{0c} and projected in wind axis using the corrected AoA α_c. Finally, forces' increments given by Equations (9), (10) and (11) are added. In the following, all corrected terms are subscripted with a *c*.

3.6 | Detection of Transition With Infrared Measurement

Infrared (IR) thermographic measurements were used to locate the laminar-turbulent transition of the boundary layer. The principles of the technique used are described in [36]. In the present experiment, two IR cameras were used, one for the lower side (FLIR SC7650 camera, IR band 1.5 to 5 μm) and one for the upper side (IRC 960 camera, IR band 2.5 to 5.1 μm). The model was covered with an insulating, high-emissivity sheet made of multiple layers of PVC, and presenting a thickness of 0.08 to 0.1 mm once applied. This black sheet is visible in Figure 1. It was found to be easy to apply and remove.

In order to generate a difference in temperature between laminar and turbulent areas that is large enough to be detected by the cameras, the total temperature of the flow is varied by about 2°C to 6°C during the wind tunnel run, by turning on or off the wind tunnel cooler. This creates a thermal imbalance between the flow and the model, causing its surface temperature to evolve to adapt to the flow temperature. Because the heat flux is considerably larger in turbulent areas, their surface temperature changes more rapidly than it does in laminar areas, which is sufficient to observe the transition. With this technique, there is no need to provide internal heating to the model as in [37], and it does not require special temperature sensitive paint as in [38]. An example of IR visualization is presented in Figure 5. It presents a turbulent wedge due to a localized roughness that spontaneously disappears for $\alpha_c > -5°$.

3.7 | Oil Flow Visualization

Oil flow visualization was performed under UV light, using mineral oil colored with titanium oxide, similar to the techniques described in [39]. The model, once covered with the sheet described in Section 3.6, is painted with a different color on the lower and upper side to better visualize mixing near the trailing edge. The black covering sheet offers good contrast with the colored oil that is gleaming under UV light. It also prevents oil from leaking into the pressure taps or model structure. The oil flow images are very efficient in accurately localizing area of separated flow, laminar bubbles and even transition to turbulence in some instances.

3.8 | XFoil Simulations

To support the analysis of the experimental results and to perform comparisons in Section 5, simulations of the airfoils under test were carried out using the XFoil 6.99 software [40]. The simulations are based on weakly compressible inviscid flow theory, coupled to 2D integral boundary layer calculations. Natural transition of the boundary layer was accounted for, with a N -factor of 9, in line with the low turbulence of the F2 and TUD-LTT wind tunnels (see Sections 2.2 and 2.4).

4 | Experimental Results

4.1 | Use of Wall Pressure for Wall Corrections

As shown in Section 3.5, the wall corrections are evaluated using pressure measured on the floor and ceiling of the wind tunnel. This method was proposed a long time ago to determine solid and wake blockage interference (see [32], p. 81),

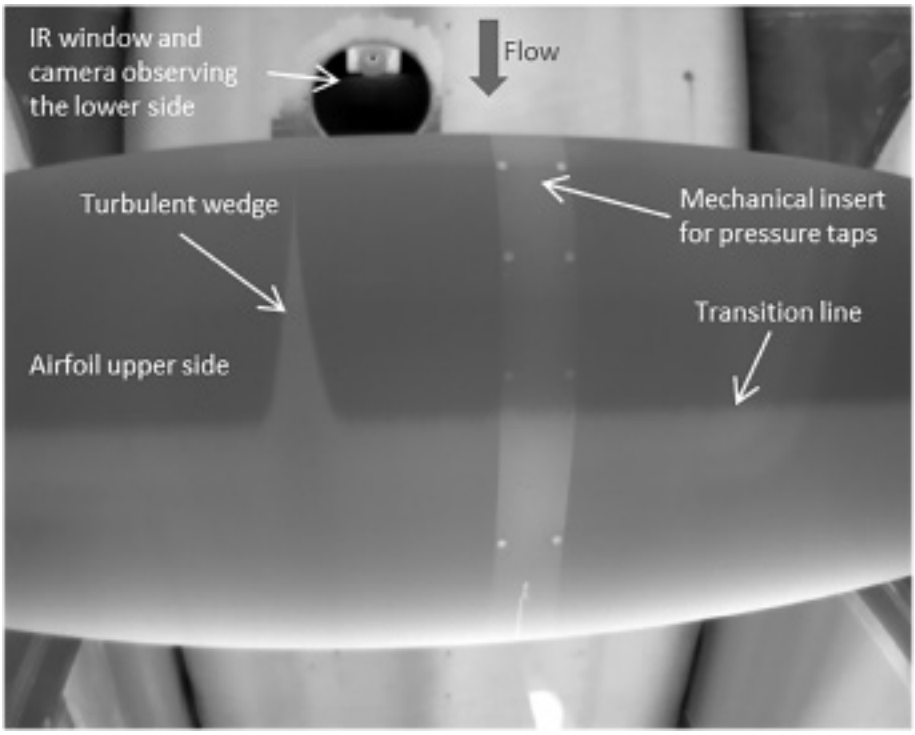

FIGURE 5 | Picture from IR camera observing the airfoil upper side at $Re_{0c} = 3.7 \times 10^6$, $\alpha = -6.5°$.

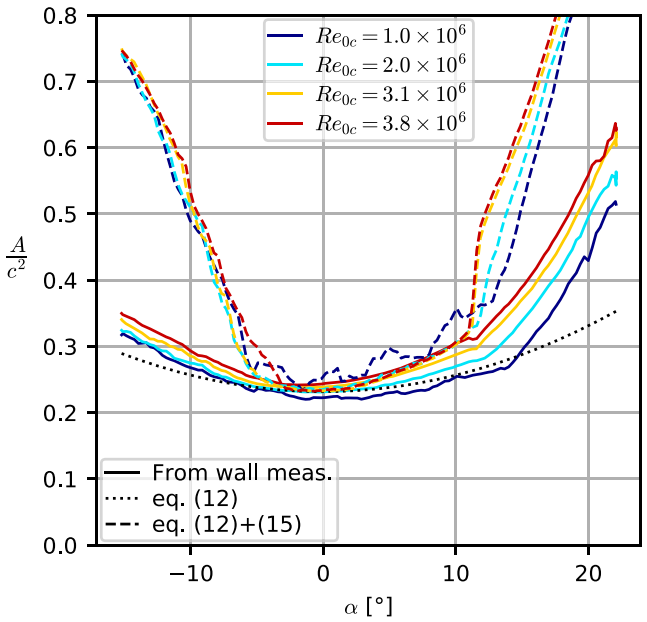

FIGURE 6 | Effective cross-section A, normalized with c^2, as a function of AoA α, according to current wall pressure measurements, used to perform regression according to Equation (3) and compared with theoretical formulation according to Equations (12) and (15).

and it is a good way to overcome the shortcomings of the potential flow model (as already discussed in [21], §5.6). Some of these shortcomings can be amplified by the large thickness ratio of the airfoil.

For example, there exist many relationships, more or less complex and empirical, between the actual airfoil shape and the effective cross-section A that determine solid blockage effects (see Equations 4 and 11). Several of these relationships are reported in AGARDograph AG-109 [21] or [24], but with only limited indications about which one is best suited for different situations.

Figure 6 shows how the effective cross-section evolves with the AoA. Focusing first on the low AoA range for which the airfoil is not stalled, the best performing formulation in the present case is eq. 5.9 in [21], complemented by the dependency to the AoA given by eq. 5.15, also in [21]. This formulation is also provided in [24], eqs. 22 and 28 and is reproduced hereafter, with A_{geom} being the geometrical cross-section of the airfoil:

$$\frac{A}{c^2} = \left(1 + 1.2\beta\frac{t}{c}\right)\left(1 + 1.1\frac{c}{t}\beta\alpha^2\right)\frac{A_{\text{geom}}}{c^2}. \tag{12}$$

In order to put things into perspective regarding the exact value of A/c^2, at low AoA, a 50% increase of this value changes the corrected velocity by about 0.6%, close to experimental uncertainty, and maximum lift coefficient by about 0.02. Hence, as already suggested in [24], classical formulae are still appropriate to deal with the present wind tunnel setup, at least up to stall, even if the airfoil is thicker than the usual aeronautical applications.

At higher AoA, either positive or negative, the stall of the airfoil gives rise to a region of separated flow that occupies a significant volume of the test section and is inaccessible to the surrounding potential flow. This effect strongly increases the effective cross-section, as can be observed in Figure 6 above 12° and below −5°. This increase is usually correlated to an increase C_{D_M} in uncorrected drag coefficient, which forms the basis of Maskell's

method [41, 42]. According to this method, the relative increase in dynamic pressure due to separated flow writes as ([24], eqs. 68 and 69, [42], eqs. 9 and 12)

$$\frac{q_M}{q} - 1 = \frac{1}{2}\left(-1 + \sqrt{1 + 4\theta \frac{c}{H} C_{D_M}}\right), \tag{13}$$

where θ is a blockage factor connected to the pressure coefficient in the separated flow area and is close to 1 for 2D flow. This is easily translated into a blockage coefficient ϵ_M by

$$\epsilon_M = \frac{1}{2 - M^2}\left(\frac{q_M}{q} - 1\right). \tag{14}$$

This blockage coefficient can itself be translated into an effective volume using Equation (4) to finally obtain

$$\frac{A_M}{c^2} = \frac{3}{\pi}\frac{\beta^3}{2 - M^2}\left(\frac{H}{c}\right)^2\left(-1 + \sqrt{1 + 4\theta \frac{c}{H} C_{D_M}}\right). \tag{15}$$

This additional effective cross-section A_M due to the volume occupied by flow separation, computed from Maskell's method, should be added to the effective cross-section of the airfoil without flow separation. The increase in drag coefficient associated to flow separation C_{D_M} is taken as the uncorrected drag coefficient, minus the minimum drag coefficient of the polar curve: $C_{D_M} = C_D - C_{D,\min}$, as measured from the wall pressures.

It can be observed in Figure 6 that the increase of blockage computed from the wall pressure is not in agreement with the usual Maskell method beyond stall. The ability of the present wall pressure method to deal with larger AoA and stalled airfoils therefore needs to be further evaluated. It is possible that the airfoil model of Section 3.5 becomes insufficient to properly capture the wall pressure distribution (see curve at $\alpha_c = 20°$ in Figure 4) and that a more elaborate model with more singularities (as in [33, 34]) would be needed. It is also observed that the doublet modeling the solid blockage moves aft of the airfoil (see values of X_μ/c in Figure 7), so that Equation (4), which expresses the blockage factor at the location of the doublet, becomes less appropriate for the airfoil location.

4.2 | Use of Wall Pressure for Measurement of Forces

Beyond deriving improved wall corrections, the regression of wall pressure measurement also delivers estimates for the airfoil force coefficients as explained in Section 3.5. It is therefore interesting to compare this wall-based estimates to the other measurements, namely the lift, pitching moment and pressure drag derived from the airfoil surface pressures (Section 3.3) and the drag derived from the wake rake (Section 3.4). This comparison is shown in Figure 7, in terms of uncorrected force coefficients.

When the airfoil is not stalled, the lift coefficient derived from wall measurements is very close (better than 0.03) to the one obtained from airfoil pressures. Immediately after stall ($\alpha > 11°$ or $\alpha < -5°$), the flow arranges itself in stall cells, the number of which depends on the aspect ratio of the model. In these circumstances, the highly three-dimensional flow pattern makes the wake rake drag and the lift from the surface pressure distribution depend on the span location. It seems logical, and measurements seem to corroborate this, that the lift from the wall distribution gives an integrated image of the forces on the model (just as balance measurements would do) and is therefore more representative of the span-averaged value. Deeper into stall, the flow obviously is still three-dimensional; however, specific patterns like the mushroom-shaped stall cells have disappeared. In these cases, with sufficient averaging time, the airfoil pressures again give sufficient accuracy for lift determination, see [24], and the lift coefficient for $\alpha > 20°$ in Figure 7.

Regarding drag, measurements based on the surface pressures lack the friction component and are consequently smaller than the total drag measured by the rake. Their accuracy also strongly depends on the tap density. Rake measurement are generally

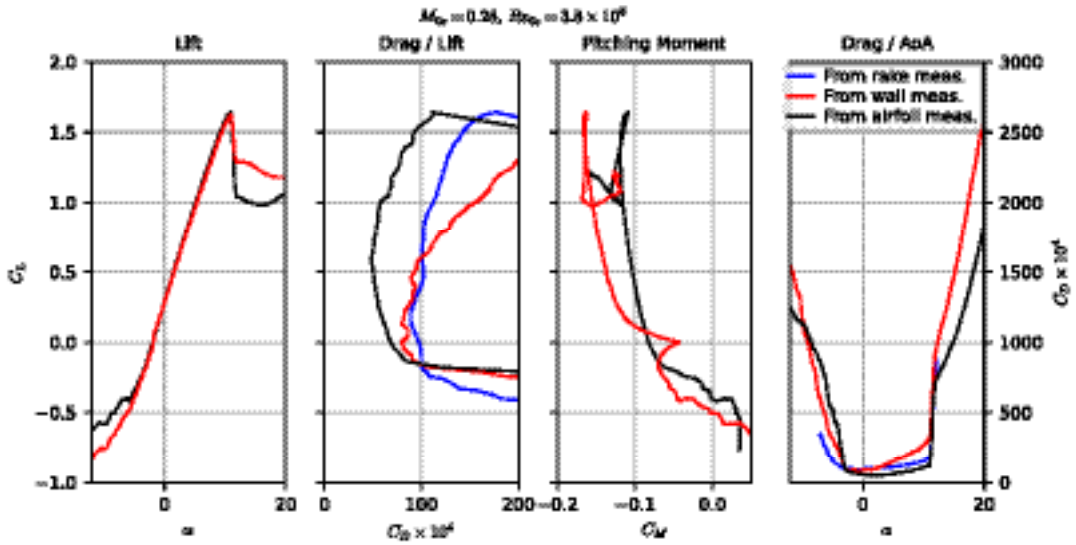

FIGURE 7 | Airfoil force coefficients (uncorrected), deduced from airfoil pressure measurements (Section 3.3), from rake pressure measurements (Section 3.4) and from wall pressure measurements (Section 3.5).

regarded as a reference, but as pointed out above, they quickly become inaccurate as the flow becomes 3D when the airfoil stalls. Drag estimates from wall measurements strongly rely on pressure coefficients measured downstream of the airfoil, where the pressure increment due to the wake displacement effect (the second term in Equation 3) becomes asymptotic and tends to the total head loss caused by the airfoil in the test section. Here again, wall-based measurement may be more representative of the span averaged drag than rake-based or airfoil-based measurements that are local to one airfoil section, and large disagreement may indicate three-dimensional flow. However, the airfoil model of Section 3.5 does not fully capture the wall pressure distribution when the airfoil is stalled, and a more elaborate model with more singularities may be needed to fully benefit from this span averaging effect.

The pitching moments derived from wall pressures show the right trend but are inaccurate compared to direct airfoil measurements, especially near zero lift. Examination of Equation (3) reveals that the pitching moment coefficient C_M does not play a role anymore in $C_{p,\text{wall}}$ when C_L approaches zero, and therefore cannot be properly identified by the regression.

This comparison again confirms that it is possible to test an airfoil not equipped with pressure taps, by using rake-based measurements for the drag of the non-stalled airfoil, and wall-based measurements for the rest of the forces, that is, lift, pitching moment and drag past stall. Such an approach was already applied in [43] for lift measurements.

4.3 | Drag Variation With Spanwise Position

A difficulty often arising in 2D airfoil testing is that in practice, the flow is never absolutely 2D over the entire span, especially at low Reynolds numbers, with the occurrence of laminar separation bubbles on the model. This is visible when performing a wake rake traverse in Y direction, at constant flow conditions and airfoil pitch angle. Such results are reported in Figure 8, for different Reynolds number and AoA. In this figure, the nominal rake position indicates where the rake was located to perform the pitch-sweep polar reported in Figure 10. Gray dashed lines also indicate the position of the port side wind tunnel wall, and the edge of the wind tunnel wall boundary layer (99% of external velocity). Each Y-traverse is actually composed of three different runs, as the range of the traverse mechanism was too limited to cover one half span of the model. On one occasion, at the highest Reynolds number tested (3.8 million), repeatability of the drag measurement at a given Y station was unsatisfactory, as can be seen in the center and right plots of Figure 8, where the curves from two different traverses do not match around $Y_s/c = -0.3$, and do not match with measurements obtained during the pitch-sweep polars. This is likely explained by the airfoil being temporarily spoiled by particles entrained in the flow. This kind of event can also be spotted in IR images; see Figure 5.

Directly in the wake of the pressure taps, at $Y_s/c = 0$, a drag increase sometimes exists in the present experiment as in [44]. It is probably related not to the pressure taps themselves, but to the surface finish of the holes used to access the screws of the mechanical insert. During model preparation, these holes were filled with plaster and carefully sanded. This nevertheless left some surface flaws, which triggers early transition when the Reynolds number becomes high enough, here above 2 million. However, this early transition does not show up in IR pictures, probably because the surface smoothness is somehow improved by the covering sheet applied on the airfoil; see Section 3.6.

When approaching the tunnel walls, part of the side wall boundary layer gets entrained in the wake which strongly increases the drag measurements, especially at low Reynolds numbers.

Outside this perturbed areas of limited extent, a scatter of about 20 to 30×10^{-4} is observed. A scatter of 10 to 15×10^{-4} along the span of the airfoil is not unusual, as can be examined from [44], fig. 8 (13×10^{-4}); from [15], fig. 4 (12 to 40×10^{-4}); or from [4], fig. 4 without VGs (12×10^{-4}). A similar plot recently obtained in the TUD-LTT for about the same AoA (unpublished data) is provided in Figure 9 for comparison and again shows a scatter of 10 to 15×10^{-4}. Figure 8 shows that some of the drag fluctuation patterns (local humps and a weak increasing trend with Y_s) are conserved from one run to another, even at different

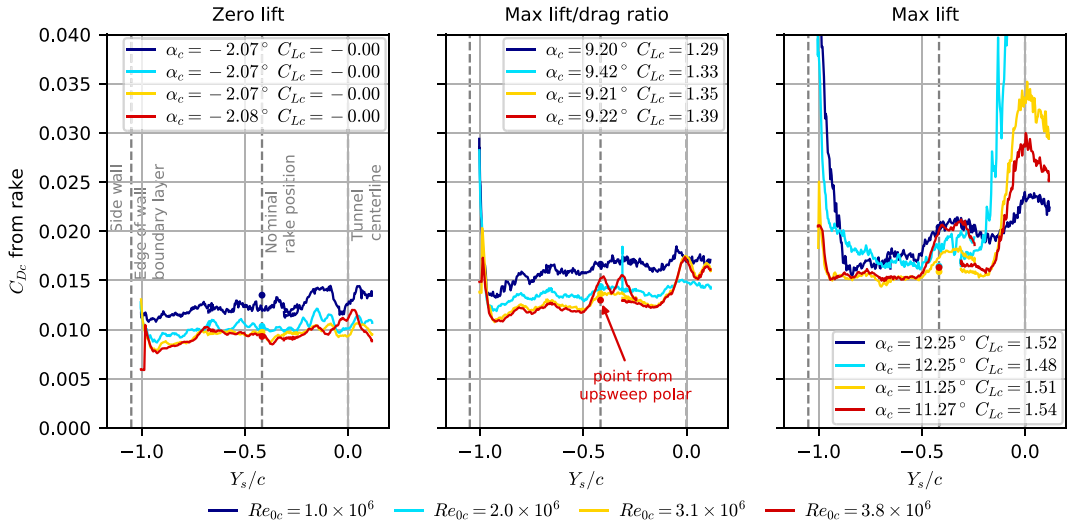

FIGURE 8 | Drag coefficient measured with the drag rake, as a function of rake lateral position Y_S.

Reynolds numbers, and are therefore not random. It is supposed at the moment that they originate from small preexisting non-uniformities in the upstream flow. In the coming years, the F2 wind-tunnel will undergo a refurbishment of its settling chamber, and the experiment will be repeated afterwards to observe if the situation has improved. Other improvements in drag measurements may include considering the flow downwash in the wake to line up the rake with the local flow.

4.4 | Clean Airfoil Performance With Reynolds Effect

This section gives an overview of results obtained from the experiment in the F2 wind tunnel, for Reynolds numbers between 1 and 3.8 millions.

4.4.1 | Force Coefficients

Figure 10 summarizes forces on the airfoil. It can be seen that the maximum lift coefficient does not evolve significantly as the Reynolds number increases, a result that is in agreement with previous findings on this airfoil [20]. The increase in lift slope is an effect of compressibility, in agreement with the Prandlt-Glauert rule. The maximum lift to drag ratio increases with the Reynolds number, as was observed in previous experiments in TUD, but surprisingly not in KKK, as discussed in [20]. Investigations on Reynolds number effect on other thick wind turbine airfoils can be found in [45, 46]. Down-sweep runs do not reveal a large hysteresis effect on stall, provide an impression of the short term repeatability of the measurement, and prove the good synchronisation between pressure and AoA measurements. In Figure 10, the drag curve at the lowest Reynolds number exhibits a larger scatter due to random fluctuations. This originates from the fact that the dynamic pressure of the flow is small compared to sensor capacity, see also Figure 3. This could have been improved by using a smaller pitch rate and increased data filtering.

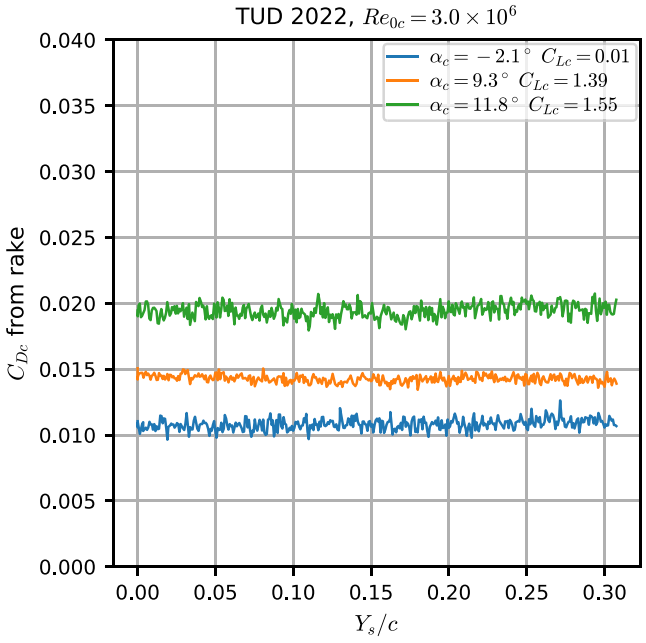

FIGURE 9 | Drag coefficient measured with the wake rake, as a function of rake span position Y_S, in TUD 2022 experiment (see Table 2). The traverse starts at 429 mm from the test section lower wall.

4.4.2 | Airfoil Pressure Distributions

The distribution of pressure coefficients on the airfoil surface is plotted in Figure 11, for different AoA. At $Re_{0c} = 1 \times 10^6$, the sudden drop in pressure coefficient observed near $x/c = 0.4$ on the lower side and $x/c = 0.3$ on the upper side are related to laminar bubbles occurring on the airfoil and also visible in oil flow pictures. They are also predicted by XFoil calculations and progressively disappear at higher Reynolds numbers.

Stall behavior at high AoA also evolves with Reynolds number. When increasing the Reynolds number, IR images reveal that the boundary layer on the suction side transitions to turbulence earlier along the chord. It then gets thicker and less able to sustain the recompression, so that flow separation occurs more upstream than at lower Reynolds number. For example, at $Re_{0c} = 10^6$ and $\alpha_c = 16°$, transition occurs at $x/c = 17\%$ and separation at $x/c = 36\%$, whereas at $Re_{0c} = 3.7 \times 10^6$ and $\alpha_c = 16°$, transition occurs at $x/c = 11\%$ and separation at $x/c = 25\%$. This explains why the flow separation gets larger at higher Reynolds number, see rightmost part of Figure 11. It also explains why the drag increases with Reynolds number past stall, see Figure 10, and so does the blockage correction, see Figure 6.

At low AoA, the flow tends to separate on the airfoil lower surface near $x/c = 30\%$, a behavior also observed in [20] and responsible for the lift and drag behavior for $\alpha < -5°$ visible in Figure 10. Although this mechanism was not specifically under study during this test, a likely explanation can be provided after examination of oil flow picture taken at $\alpha = -2°$ shown in Figure 12. In this picture, the flow is laminar upstream of the separation bubble that is clearly visible near $x/c = 30\%$, then it transitions to turbulent through a laminar separation bubble, and keeps attached further downstream until the trailing edge. However, from place to place, turbulence is locally triggered upstream of the laminar bubble by unidentified obstacles (possibly introduced by the oil painting or by particles entrained in the tunnel flow). Downstream of each turbulent wedge, the laminar bubble disappears and the turbulent flow separates downstream. A similar situation is observed with IR images, see Figure 13, where the turbulent wedge on the left hand side of the picture caused a massive separation that distorts the transition line across about a quarter of the model span. Since the pressure taps introduce some surface imperfections as previously described in Section 4.3, turbulent wedges are likely to form and to promote separation near the row of pressure taps used to compute airfoil forces. As the Reynolds number increases, the boundary layer gets more and more receptive to these surface flaws, thus explaining the Reynolds number dependency observed in Figures 10 and 11. Otherwise, the flow remains very much two dimensional, including close to the tunnel side walls, see Figure 12, in spite of the absence of any device to control the boundary layer on the tunnel walls.

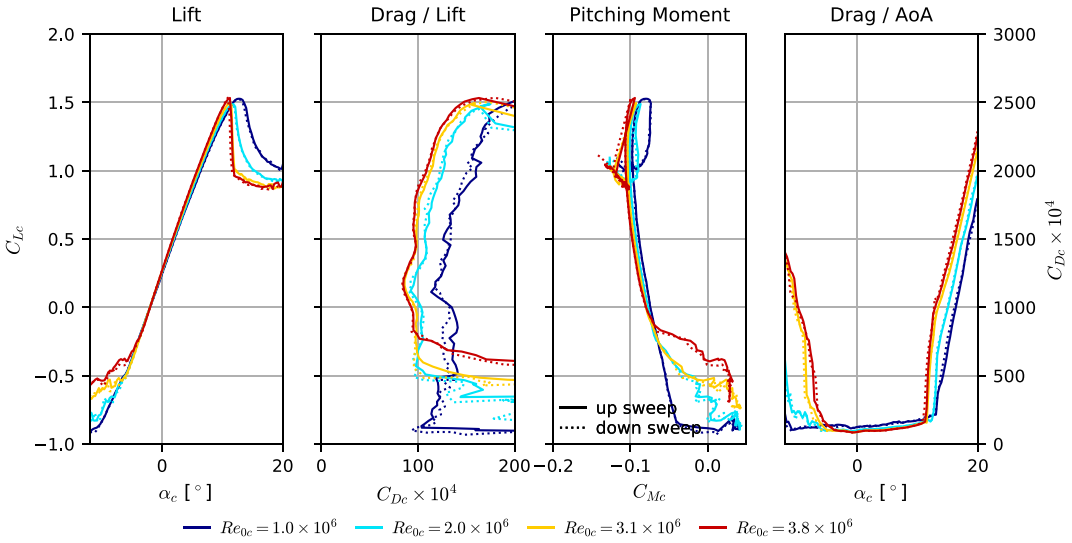

FIGURE 10 | Force coefficients for the clean airfoil.

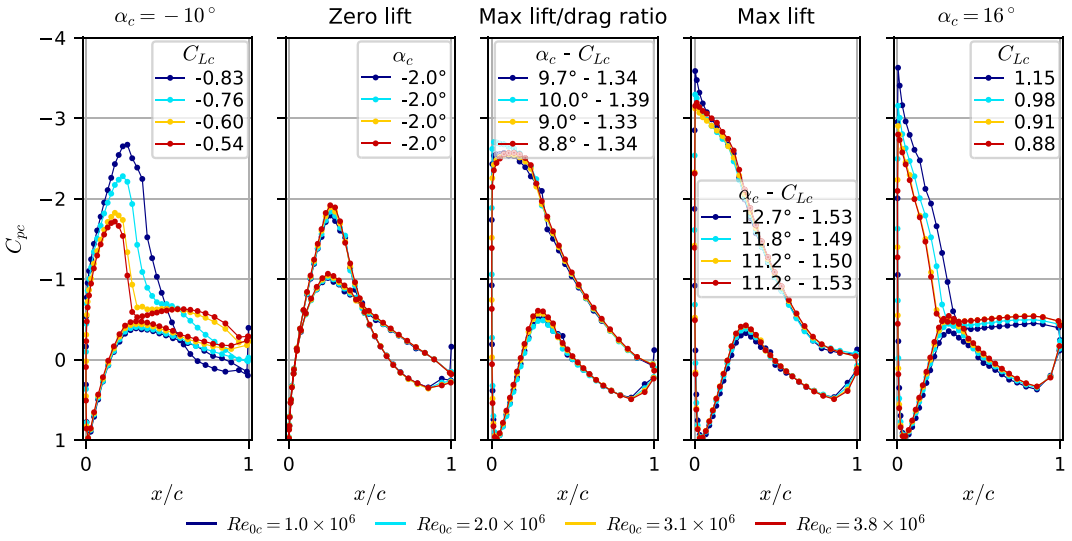

FIGURE 11 | Pressure distribution on the clean airfoil.

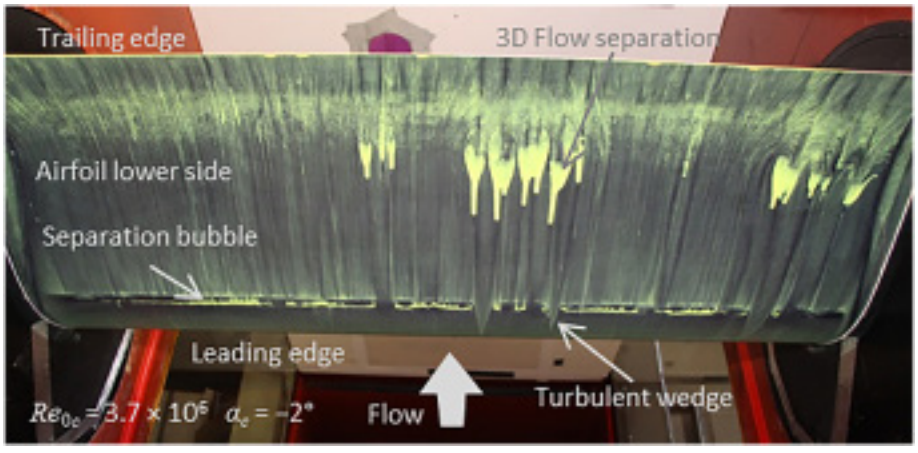

FIGURE 12 | Oil flow picture of the lower side of the airfoil, immediately after a run at $Re_{0c} = 3.7 \times 10^6$ and $\alpha_c = -2°$.

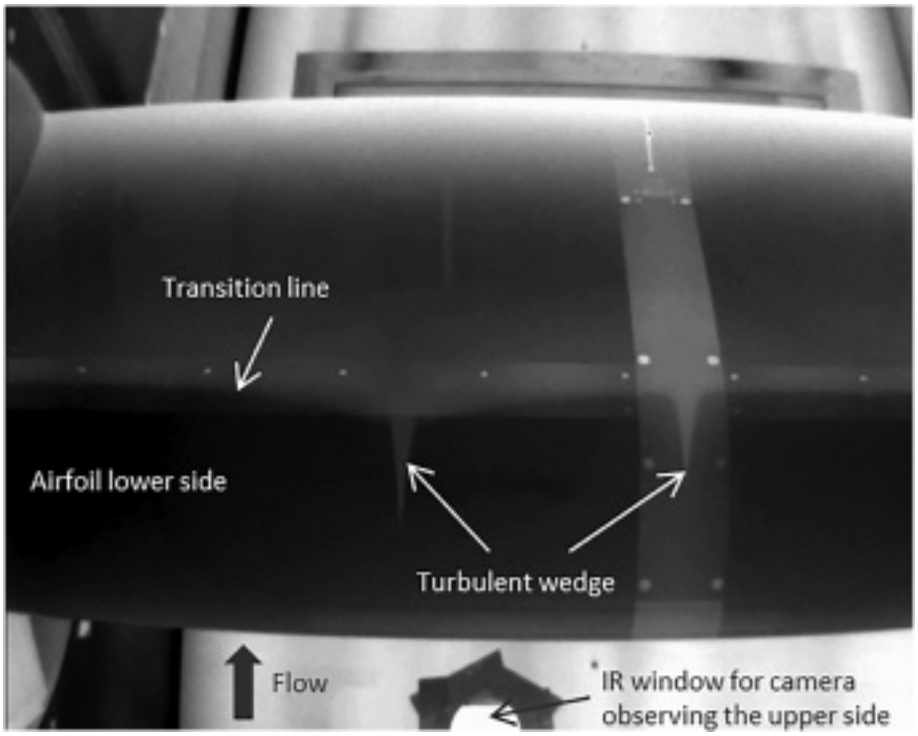

FIGURE 13 | IR picture of the lower side of the airfoil, during a run at $Re_{0c} = 3.7 \times 10^6$, at $\alpha_c = -7°$.

TABLE 2 | Summary of the different wind tunnel experiments under consideration.

Label	Tunnel name	Tunnel size $B \times H$	Airfoil chord c (c/H, c/B)	Airfoil shape	Reference
F2	ONERA F2	1.4 m × 1.8 m	0.60 m (0.33, 0.43)	DU 97-W-300Mod	Present paper
KKK	DNW Kryo Kanal Köln	2.4 m × 2.4 m	0.50 m (0.21, 0.21)	DU 97-W-300Mod	[11, 20]
TUD 1997	Low turbulence tunnel	1.25 m × 1.8 m, octagonal	0.65 m (0.36, 0.52)	DU 97-W-300	[20, 22]
TUD 2017					[4]
TUD 2022					Present paper
XFoil (DU 97-W-300)	N/A	N/A	N/A	DU 97-W-300	[40]
XFoil (DU 97-W-300Mod)				DU 97-W-300Mod	

5 | Comparison With Previous Experiments

Comparing results between different facilities is a common practice in experimental science. Regarding airfoil testing, this method was applied on the NACA0012 airfoil by McCroskey [47]. It helped pointing out the limits and uncertainties of the experiments at the time, but also helped reinforcing some experimental facts. For example, the value of maximum lift coefficient as a function of Reynolds and Mach number was found to be consistent across many experiments, which contradicted "conventional widsom" that it was nearly impossible to obtain a consistent stall behavior in 2D experiments.

Comparisons between experiments dealing with thicker wind turbine dedicated airfoils are presented in [26, 44, 46, 48], some involving the TU Delft wind tunnel as in the present paper, and some other facilities. Data available from previous experiments is summarized in Table 2. Other experimental data regarding the DU 97-W-300 airfoil are presented in [49], but with a very unconventional model setup that appears to be far from 2D testing, and that were consequently not considered for comparison.

For this comparison, flow conditions as close as possible to a Reynolds number of 2 millions, common to all experiments, were selected. Similar plots and conclusions were also obtained with a Reynolds number of 3 millions.

5.1 | Force Coefficients

An overview of forces coefficients is provided in Figure 14, and some statistics are provided in Figure 15. In this figure,

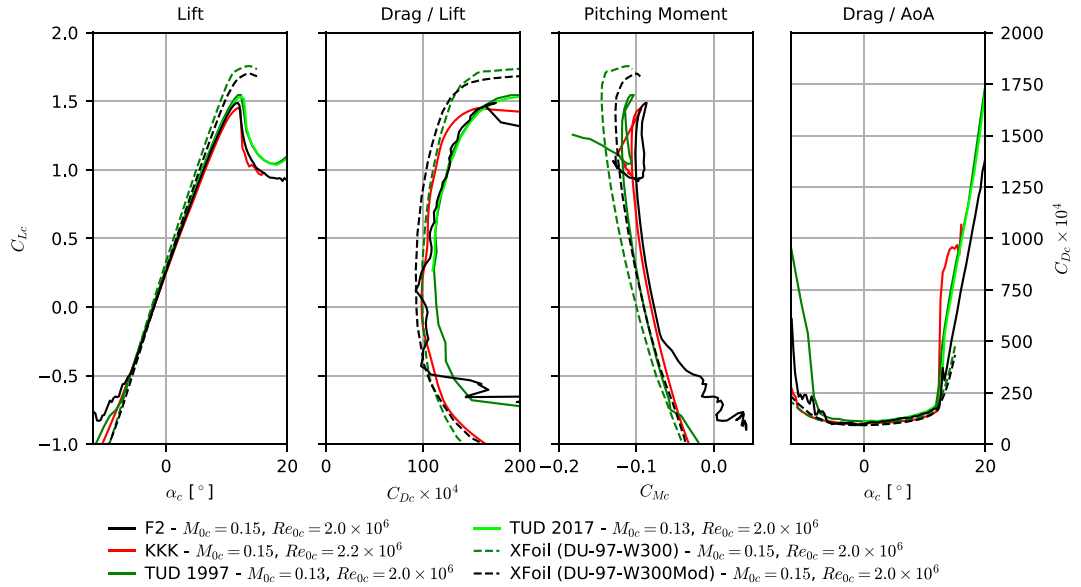

FIGURE 14 | Comparison of force coefficients on clean airfoil with previously published experiment.

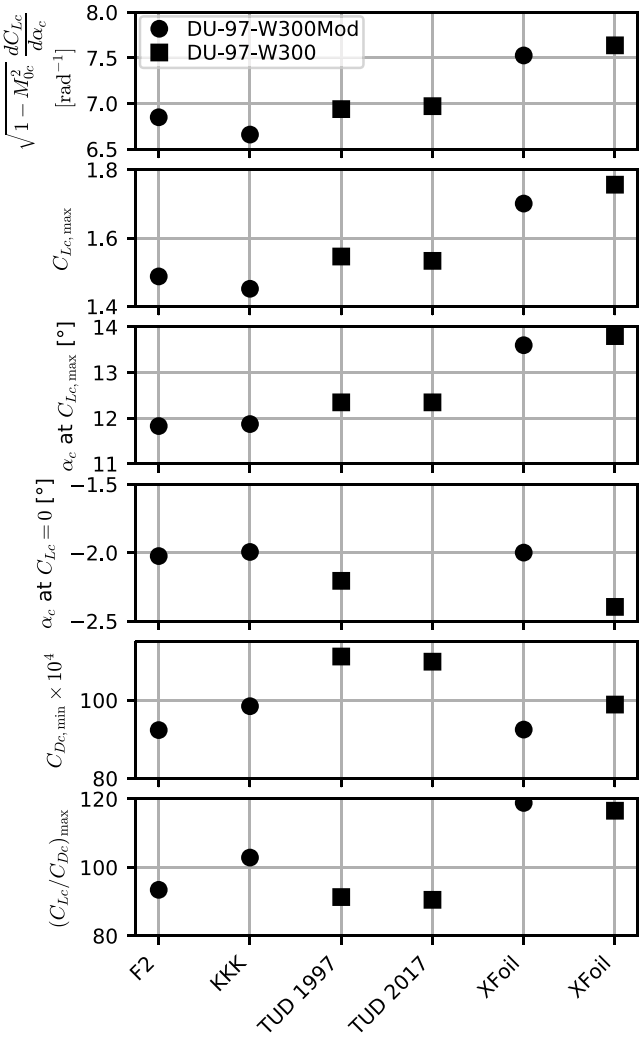

FIGURE 15 | Some statistics regarding force coefficients on clean airfoil, according to present and previously published experiments.

the lift slope $\frac{dC_{Lc}}{d\alpha_c}$ is computed with the help of a linear regression of data within $-2° \leq \alpha_c \leq +7°$, then multiplied by the factor $\sqrt{1-M_{0c}^2}$ to remove compressibility effects due to the slightly different Mach numbers. When comparing experiments, one has to bear in mind that the airfoil tested in the TUD-LTT is the original DU 97-W-300, whereas the one tested in F2 and KKK is a modified version (see Section 2.1 and Table 2). Simulations of both airfoils, carried out with XFoil, are also provided in the figures.

The experiment in KKK benefits from the smallest chord to span ratio c/B and chord to height ratio c/H, which should make it less sensitive to three dimensional effects and uncertainties in wall corrections. Present experimental results in F2, as well as results in TUD, exhibit a lift slope and a maximum lift coefficient 2% to 3% higher as well. AoA at zero lift (α_c at $C_{Lc} = 0$) and AoA at stall (α_c at $C_{Lc} = C_{Lc,\max}$) are in good agreement across experiments, with differences smaller than 0.4°. Moreover, one can note in Figure 15 that the small lift differences between F2 and TUD can be explained by differences in airfoil shape, according to XFoil predictions. This is especially true of the lift slope and AoA at zero lift, two parameters that should be easier to predict with flow simulations. On the basis of the many KKK measurement results on this airfoil, it was suggested in [11] that the cooling process of the tunnel gas might have impacted the results, because of ice depositing on the model, or because of increased turbulence levels (During KKK measurements displayed here, the temperature of the flow was $-23°C$). Another hypothesis is that the velocity during KKK experiment was overestimated by about 1.2%, which would also explain the differences in pressure distribution reported in the next section.

Drag results show a larger scatter across experiments. The minimum drag coefficient in F2 and KKK lies between 92

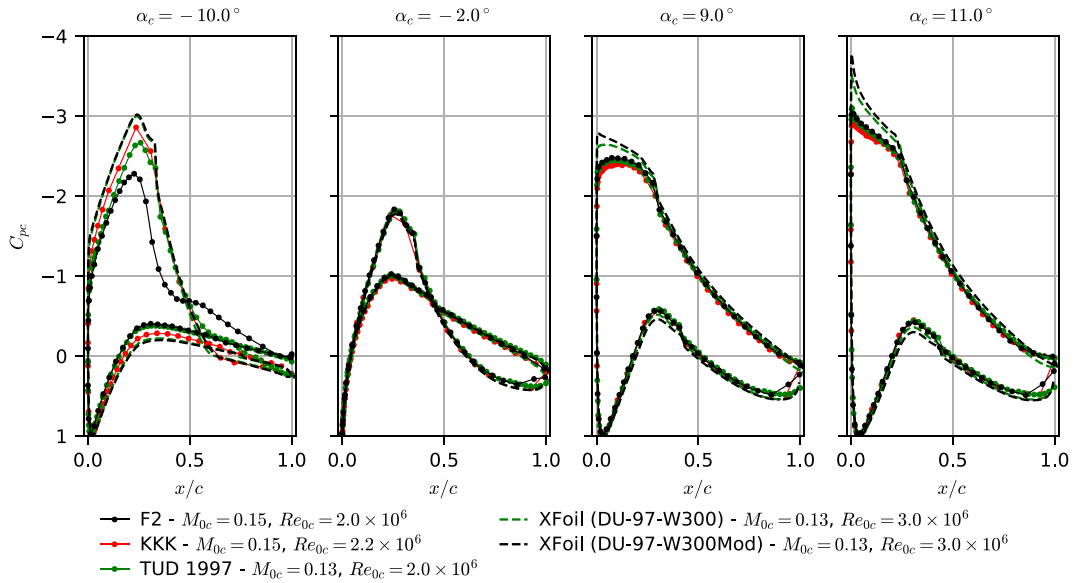

FIGURE 16 | Comparison of pressure distribution on clean airfoil with previously published experiment.

and 98×10^{-4}, quite close to XFoil prediction. At higher AoA, the drag measurements in F2 and TUD are in agreement, and drag rises at a faster pace than predicted with XFoil and KKK. Consequently the maximum lift-to-drag ratio $(C_{Lc}/C_{Dc})_{\max}$ is about 92 for F2 and TUD, 103 for KKK and almost 120 for XFoil.

The post-stall behavior is also somewhat different, with a larger and more sudden loss of lift in F2 and KKK experiments, and different drag rise past $\alpha_c = 13°$. The main issue, though, is related to the three-dimensional nature of the flow, that cannot be measured by the airfoil pressure taps because they are inherently local to the center section of the model. As already suggested in Section 4.2, more representative values may be obtained from the wall pressure measurements.

5.1.1 | Airfoil Pressure Coefficient

Pressure distributions on the airfoil are presented for various AoA in Figure 16. At very low AoA, the airfoil is more severely stalled in F2 than in other wind tunnels. Earlier boundary layer transition, responsible for flow separation on the lower side, as described in Section 4.4.2 is probably responsible. At higher AoA, pressure distribution is very much comparable. The suction peak is about 3% lower in KKK, which is in agreement with the reduced lift slope and max lift coefficient discussed in Section 5.1. Differences between F2 and TUD are small and can partly be explained by the differences in airfoil shape, except for one tap on the lower surface near the trailing edge which was probably malfunctioning.

5.2 | Discussion

Overall, the different experiments produce results that are close to each others in terms of lift, including maximum lift, and pitching moment, with deviations in the order of 2%–3% that are acceptable for the usage of the measurements. For comparison, in reference [47], even within the highest quality experiments (group 1), a scatter of about 5% in lift slope, and about 10% in maximum lift was observed.

Drag measurements appears to be less satisfactory, as a spread of about 20×10^{-4} is observed, that is, about 20% of the minimum drag. However, for AoA above 3° and up to stall, the agreement between F2 and TUD is much better, within 5 to 10×10^{-4} in drag coefficient. Moreover, part of this small difference can be explained by the drag penalty created by the thicker trailing edge of the original DU 97-W-300 airfoil. Consequently, the lift-to-drag ratio is also in agreement in this range of AoA for these two facilities. As previously observed [50], numerical predictions with XFoil underpredict drag with increasing airfoil thickness.

Post stall behavior also presents large deviations between experiments, that could not be explained, although three-dimensional effect are suspected to play a key role.

6 | Conclusion

An extensive experimental characterization of the DU 97-W-300Mod airfoil was undertaken in the ONERA F2 wind tunnel. Experimental techniques were presented, in particular, the use of wind tunnel wall pressure measurements to secure the wall corrections, and to derive forces on the airfoil, including lift, drag and pitching moment estimates. The test allowed investigating Reynolds number effects between 1 and 3.8 millions.

A special effort was devoted to compare the present results with previously published experimental data from tests on a similar model. A good agreement is observed concerning lift measurements, especially lift slope and maximum lift coefficient, with only a few percent deviations. Wake rake drag measurements, however, show considerable scatter, both in span wise direction within the present experiment, and across experiments, with deviations in the order of 20% of minimum drag. A better

agreement, within 5 to 10×10^{-4} in drag coefficient was however obtained between F2 and TUD data in a large and important range of incidences.

It is hoped that this paper will help advancing wind tunnel techniques in thick 2D airfoil testing, where a number of factors can jeopardize the accuracy of the measurements, among which: early transition caused either by small-scale surface roughness or by free stream turbulence, local flow in-homogeneity, proper tunnel calibration, wall corrections and three-dimensional effects at stall.

Author Contributions

Sylvain Mouton: supervision, investigation, methodology, writing–original draft. **Alois Peter Schaffarczyk:** writing–review and editing. **Nando Timmer:** investigation, writing–review and editing.

Conflicts of Interest

The authors declare no conflicts of interest.

Data Availability Statement

Authors elect to not share data.

Peer Review

The peer review history for this article is available at https://www.webofscience.com/api/gateway/wos/peer-review/10.1002/we.2938.

References

1. Y. Shulong, C. Mayank, T. Griffith, et al., "Aero-Structural Design and Optimization of 50-MW Wind Turbine With Over 250-m Blades," *Wind Engineering* 46, no. 1 (2022): 273–295.

2. P. F. Bernhard Stoevesandt and S. Yuping eds., *Handbook of Wind Energy Aerodynamics* (Springer, 2021).

3. H. Knobbe-Eschen, J. Stemberg, K. Abdellaoui, et al., "Numerical and Experimental Investigations of Wind-Turbine Blade Aerodynamics in the Presence of Ice Accretion," AIAA Scitech 2019 Forum: 805, https://arc.aiaa.org/doi/abs/10.2514/6.2019-0805.

4. D. Baldacchino, C. Ferreira, D. De Tavernier, W. A. Timmer, and G. J. W. van Bussel, "Experimental Parameter Study for Passive Vortex Generators on a 30% Thick Airfoil," *Wind Energy* 21, no. 9 (2018): 745–765, https://onlinelibrary.wiley.com/doi/abs/10.1002/we.2191.

5. L. Gao, H. Zhang, Y. Liu, and S. Han, "Effects of Vortex Generators on a Blunt Trailing-Edge Airfoil for Wind Turbines," *Renewable Energy* 76 (2015): 303–311, https://www.sciencedirect.com/science/article/pii/S0960148114007587.

6. A. P. Schaffarczyk and C. Arakawa, "A Thick Aerodynamic Profile With Regions of Negative Lift Slope and Possible Implications on Profiles for Wind Turbine Blades," *Wind Energy* 24, no. 2 (2021): 162–173, https://onlinelibrary.wiley.com/doi/pdf/10.1002/we.2565.

7. A. P. Schaffarczyk, "Corrections and Uncertainties," *Handbook of Wind Energy Aerodynamics*, eds. B. Stoevesandt, G. Schepers, P. Fuglsang, and S. Yuping (Springer International Publishing, 2020), 1–12.

8. O. Ceyhan Yilmaz, "Examples of Wind Tunnels for Testing Wind Turbine Airfoils," *Handbook of Wind Energy Aerodynamics*, eds. B. Stoevesandt, G. Schepers, P. Fuglsang, and S. Yuping (Springer International Publishing, Cham, 2020), 1–28.

9. C. Bak, "Aerodynamic Design of Wind Turbine Rotors," *Advances in Wind Turbine Blade Design and Materials* (Woodhead Publishing Ltd., Cambridge, UK, 2013), 59–108.

10. E. Gaernter, J. Rinker, L. Sethuraman, et al., "Definition of the IEA Wind 15-Megawatt Offshore Reference Wind Turbine," NREL/TP-5000-75698. NREL, Golden, CO, USA, (2020).

11. W. A. Timmer and R. P. J. O. M. van Rooij, "Summary of the Delft University Wind Turbine Dedicated Airfoils," *Journal of Solar Energy Engineering* 125, no. 4 (2003): 488–496, https://doi.org/10.1115/1.1626129.

12. W. A. Timmer and R. P. J. O. M. van Rooij, "Summary of the Delft University Wind Turbine Dedicated Airfoils," 41st Aerospace Sciences Meeting and Exhibit, (2003), https://arc.aiaa.org/doi/abs/10.2514/6.2003-352.

13. H. J. T. Kooijman, C. Lindenburg, D. Winkelaar, and E. L. Van der Hooft, "Dowec 6 MW Pre-Design," ECN-CX–01-135. ECN, Petten, The Netherlands, (2003).

14. B. R. Resor, "Definition of a 5 MW/61.5 m Wind Turbine Blade Reference Model," SAND2013-2569. SANDIA; Albuquerque, NM, USA, (2013).

15. V. S. Alois Peter Schaffarczyk, "Wind Tunnel Investigations of DU 97-W-300-mod Equipped With Riblets," *Wind Energy* 24, no. 10 (2021): 1156–1161, https://onlinelibrary.wiley.com/doi/abs/10.1002/we.2622.

16. O. Ceyhan, O. Pires, X. Munduate, et al., "Summary of the Blind Test Campaign to Predict the High Reynolds Number Performance of DU00-w-210 Airfoil," 35th Wind Energy Symposium, 915.

17. M. F. D Afchain and G. Rancarani, "La soufflerie F2 du centre du fauga-mauzac (the F2 wind-tunnel of the fauga-mauzac center)," NASA-TM-77482, 1984. Association Aéronautique et Astronautique de France (AAAF), (1983), https://hal.archives-ouvertes.fr/hal-03224322.

18. J. M. Christophe, "The F2 Wind Tunnel of the Fauga-Mauzac Test Center," 15th Congress of the International Council of the Aeronautical Sciences (The International Council of the Aeronautical Sciences, 1986): 923–933.

19. F. Nicolas, D. Donjat, A. Plyer, et al., "Experimental Study of a Co-Flowing Jet in ONERA's F2 Research Wind Tunnel by 3D Background Oriented Schlieren," *Measurement Science and Technology* 28, no. 8 (2017): 85302.

20. W. A. Timmer and A. P. Schaffarczyk, "The Effect of Roughness at High Reynolds Numbers on the Performance of Aerofoil DU 97-W-300Mod," *Wind Energy* 7, no. 4 (2004): 295–307, https://onlinelibrary.wiley.com/doi/abs/10.1002/we.136.

21. H. C. Garner, E. Rogers, W. E. A. Acum, and E. C. Maskell, "Subsonic Wind Tunnel Wall Corrections," AGARDograph No. 109. RTO/NATO, (1966).

22. R. P. J. O. M. van Rooij and W. A. Timmer, "Roughness Sensitivity Considerations for Thick Rotor Blade Airfoils," *Journal of Solar Energy Engineering* 125, no. 4 (2003): 468–478, https://doi.org/10.1115/1.1624614.

23. O. Ceyhan Yilmaz and W. A. Timmer, "Experimental Evaluation of a Non-Conventional Flat Back Thick Airfoil Concept for Large Offshore Wind Turbines," 2018 AIAA Applied Aerodynamics Conference, 3827.

24. W. A. Timmer, "Wind Tunnel Wall Corrections for Two-Dimensional Testing up to Large Angles of Attack," *Handbook of Wind Energy Aerodynamics*, eds. B. Stoevesandt, G. Schepers, P. Fuglsang, and S. Yuping (Springer International Publishing, Cham, 2021), 1–29.

25. S. H. Chue, "Pressure Probes for Fluid Measurement," *Progress in Aerospace Sciences* 16, no. 2 (1975): 147–223.

26. M. S. Kuester, K. Brown, T. Meyers, N. Intaratep, A. Borgoltz, and W. J. Devenport, "Wind Tunnel Testing of Airfoils for Wind Turbine Applications," *Wind Engineering* 39, no. 6 (2015): 651–660, https://www.jstor.org/stable/90007101.

27. M. Méheut and D. Bailly, "Drag-Breakdown Methods From Wake Measurements," *AIAA Journal* 46, no. 4 (2008): 847–862, https://doi.org/10.2514/1.29051.

28. B. Jones, "Measurement of Profile Drag by the Pitot-Traverse Method," R&M 1688. British Aeronautical Research Council, (1936).

29. C. N. H. Lock, S. Goldstein, and W. F. Hilton, "Determination of Profile Drag at High Speeds by Pitot Traverse Methods," R&M1970. British Aeronautical Research Council, (1940).

30. B. F. R. Ewald ed. "Wind Tunnel Wall Corrections," AGARDograph No. 336. RTO/NATO, (1998).

31. S. Goldstein, "Two-Dimensional Wind-Tunnel Interference," ARC R&M 1902, (1942).

32. M. Mokry, Y. Y. Chan, and D. J. Jones, "Two-Dimensional Wind Tunnel Wall Interference," AGARDograph No. 281. RTO/NATO, (1983).

33. S. R. Allmaras, "On Blockage Corrections for Two-Dimensional Wind Tunnel Tests Using the Wall-Pressure Signature Method," TM-86759. NASA, (1986).

34. L. Wang, Y. Jiao, and Y. Gao, "Airfoil Wind tunnel Correction for Angles of Attack From −180 deg to 180 deg," *Wind Energy* 18, no. 8 (2015): 1487–1500, https://onlinelibrary.wiley.com/doi/abs/10.1002/we.1771.

35. H. J. Allen and W. G. Vincenti, "Wall Interference in a Two-Dimensional-Flow Wind Tunnel, With Cconsideration of the Effect of Compressibility," TR-782. NACA, (1944).

36. Y. Le Sant, M. Marchand, P. Millan, and J. Fontaine, "An Overview of Infrared Thermography Techniques Used in Large Wind Tunnels," *Aerospace Science and Technology* 6, no. 5 (2002): 355–366.

37. L. A. Joseph, A. Borgoltz, and W. Devenport, "Infrared Thermography for Detection of Laminar–Turbulent Transition in Low-Speed Wind Tunnel Testing," *Exp Fluids* 57, no. 77 (2016), https://rdcu.be/cFOa8.

38. M. Costantini, C. Fuchs, U. Henne, et al., "Experimental Analysis of a Wind-Turbine Rotor Blade Airfoil by Means of Temperature-Sensitive Paint," AIAA Scitech 2019 forum, 800, https://arc.aiaa.org/doi/abs/10.2514/6.2019-0800.

39. R. L. Maltby ed. "Flow Visualization in Wind Tunnels Using Indicators," AGARDograph No. 70. RTO/NATO, (1962).

40. M. Drela, "Xfoil: An Analysis and Design System for Low Reynolds Number Airfoils," Low Reynolds Number Aerodynamics: Proceedings of the Conference Notre Dame, (1989), 1–12.

41. E. C. Maskell, "A Theory of the Blockage Effects on Bluff Bodies and Stalled Wings in a Closed Wind Tunnel," R&M 3400. British Aeronautical Research Council, (1963).

42. J. E. Hackett and K. R. Cooper, "Extensions to Maskell's Theory for Blockage Effects on Bluff Bodies in a Closed Wind Tunnel," *The Aeronautical Journal* 105, no. 1050 (2001): 409–418.

43. T. Kuhn, A. Altmikus, N. Balaresque, and M. Lippert, "Numerical Replication and Improvement of Wind Tunnel Tests for Design and Off-Design Operating Points of Wind Turbine Airfoils," 33rd AIAA Applied Aerodynamics Conference: pp. 2577, https://arc.aiaa.org/doi/abs/10.2514/6.2015-2577.

44. P. Fuglsang and S. Bove, "Wind Tunnel Testing of Airfoils Involves More Than Just Wall Corrections," European Wind Energy Conference and Exhibition 2008, Vol. 3, (2008): 1420–1430. Cited By: 15.

45. D. Sommers and J. Tangler, "Wind-Tunnel Tests of Two Airfoils for Wind Turbines Operating at High Reynolds Numbers," 2000 ASME Wind Energy Symposium, 43.

46. E. Llorente, A. Gorostidi, M. Jacobs, W. A. Timmer, X. Munduate, and O. Pires, "Wind Tunnel Tests of Wind Turbine Airfoils at High Reynolds Numbers," *Journal of Physics: Conference Series* 524 (2014): 12012, https://doi.org/10.1088/1742-6596/524/1/012012.

47. W. J. McCroskey, "A Critical Assessment of Wind Tunnel Results for the NACA0012 Airfoil," Technical Memorandum 100019. NASA, (1987).

48. O. Pires, X. Munduate, O. Ceyhan, M. Jacobs, J. Madsen, and J. G. Schepers, "Analysis of the High Reynolds Number 2D Tests on a Wind Turbine Airfoil Performed at Two Different Wind Tunnels," *Journal of Physics: Conference Series* 749 (2016): 12014, https://doi.org/10.1088/1742-6596/749/1/012014.

49. J. Kiefer, M. A. Miller, M. Hultmark, and M. O. L. Hansen, "Effects of Finite Aspect Ratio on Wind Turbine Airfoil Measurements," *Journal of Physics: Conference Series* 753 (2016): 22040, https://doi.org/10.1088/1742-6596/753/2/022040.

50. W. A. Timmer, "An Overview of NACA 6-Digit Airfoil Series Characteristics With Reference to Airfoils for Large Wind Turbine Blades," 47th AIAA Aerospace Sciences Meeting Including the New Horizons Forum and Aerospace Exposition, 268.